*Energies* **2010**, *3*, 1831-1860; doi:10.3390/en3121831

OPEN ACCESS

*energies*

**ISSN 1996-1073**

www.mdpi.com/journal/energies

*Article*

# A New Hybrid Algorithm Using Thermodynamic and Backward Ray-Tracing Approaches for Modeling Luminescent Solar Concentrators

**Chin Kim Lo *, Yun Seng Lim, Seng Gee Tan and Faidz Abd Rahman**

Faculty of Engineering and Science, Universiti Tunku Abdul Rahman, Jalan Genting Klang, 53300, Kuala Lumpur, Malaysia; E-Mails: yslim@utar.edu.my (Y.S.L.); tansg@utar.edu.my (S.G.T.); faidzar@utar.edu.my (F.A.R.)

* Author to whom correspondence should be addressed; E-Mail: ukwn.cklo@gmail.com; Tel.: +60-34109802 or +60-123459598.

*Received: 24 September 2010; in revised form: 12 November 2010 / Accepted: 23 November 2010 / Published: 26 November 2010*

---

**Abstract:** A Luminescent Solar Concentrator (LSC) is a transparent plate containing luminescent material with photovoltaic (PV) cells attached to its edges. Sunlight entering the plate is absorbed by the luminescent material, which in turn emits light. The emitted light propagates through the plate and arrives at the PV cells through total internal reflection. The ratio of the area of the relatively cheap polymer plate to that of the expensive PV cells is increased, and the cost per unit of solar electricity can be reduced by 75%. To improve the emission performance of LSCs, simulation modeling of LSCs becomes essential. Ray-tracing modeling is a popular approach for simulating LSCs due to its great ability of modeling various LSC structures under direct and diffuse sunlight. However, this approach requires substantial amount of measurement input data. Also, the simulation time is enormous because it is a forward-ray tracing method that traces all the rays propagating from the light source to the concentrator. On the other hand, the thermodynamic approach requires substantially less input parameters and simulation time, but it can only be used to model simple LSC designs with direct sunlight. Therefore, a new hybrid model was developed to perform various simulation studies effectively without facing the issues arisen from the existing ray-tracing and thermodynamic models. The simulation results show that at least 60% of the total output irradiance of a LSC is contributed by the light trapped and channeled by the LSC. The novelty of this hybrid model is the concept of integrating the thermodynamic model with a well-developed

Radiance ray-tracing model, hence making this model as a fast, powerful and cost-effective tool for the design of LSCs.

**Keywords:** luminescent solar concentrator; thermodynamic; backward ray-tracing

---

**Nomenclature**

*Physical Constants*

| | | | |
|---|---|---|---|
| $c$ | Speed of light in free space | $k$ | Boltzmann constant |
| $h$ | Planck constant | $q$ | Elementary charge constant |
| $n_{air}$ | Refractive index of air | | |

*LSC Properties (Input Parameters)*

| | | | |
|---|---|---|---|
| $L$ | Length of LSC | $n$ | Refractive index of LSC |
| $W$ | Width of LSC | $T$ | Temperature |
| $D$ | Thickness of LSC | $I_1$ | Incident light spectrum |
| $Q_e$ | Luminescent quantum efficiency | $\sigma_e$ | Absorption cross section of dye |
| $N$ | Number of luminescent dye particles per unit volume | $\sigma_a$ | Absorption cross section of LSC sample |

*Simulation*

| | | | |
|---|---|---|---|
| $\lambda$ | Radiation wavelength | $\theta$ | Polar angle |
| $v$ | Radiation frequency | $\varphi$ | Azimuthal angle |
| $\Phi(\lambda)$ | Spectral photon flux (wavelength domain) | $I(\nu)$ | Spectral photon flux (frequency domain) |
| $E(\lambda)$ | Spectral irradiance (wavelength domain) | $\lambda_{em\_peak}$ | Emission peak wavelength |
| $\sigma_{meas}$ | Measured absorption cross section | $I_{em\_peak}$ | Emission peak intensity |
| $\sigma_{eff}$ | Effective absorption cross section | $\Delta\lambda_p$ | Mismatch in emission peak wavelength |
| $\lambda_p$ | Absorption peak wavelength | $\Delta I_p$ | Mismatch in emission peak intensity |

*Ray-Tracing Model*

| | | | |
|---|---|---|---|
| $P_{rad}$ | Radiant power | $M_\theta$ | Number of discrete θ |
| $L$ | Radiance | $M_\varphi$ | Number of discrete φ |
| $\Omega$ | Solid angle | $M_y$ | Number of discrete points along $y$ direction |
| $r$ | Position vector | $M_z$ | Number of discrete points along $z$ direction |

*Thermodynamic Model*

| | | | |
|---|---|---|---|
| $B(v)$ | Luminescent brightness | $\mu$ | Photon chemical potential |
| $I_E(v)$ | Escaped flux | $R$ | Reflection coefficient |
| $I_T(v)$ | Trapped flux | $\theta_C$ | Critical angle |
| $\Omega_C$ | Solid angle extended by an escape cone | | |

## 1. Introduction

The luminescent solar concentrator (LSC) is a non-imaging optical device that can concentrate sunlight onto a small area of solar cells to generate electricity. In this way, a large area of solar cells required in a standard flat-plate PV panel can be replaced by an inexpensive concentrator, hence reducing the cost of the module and thus the cost per unit electricity generated [1].

The LSC typically consists of a polymer plate doped with a luminescent material, with solar cells attached to the plate edges. Figure 1 shows a diagram of the simplest type of luminescent solar concentrator. Higher efficiency can be achieved by matching the peak quantum efficiency of the solar cells to the peak emission of the concentrator. Several types of luminescent materials can be used in LSCs, such as laser dyes or organic dyes, semiconductor quantum dots [2], rare earth materials [3], and semiconducting polymers [4]. To further improve the efficiency of LSCs, materials such as photonic layers [5] and liquid crystals [6] have also been used to reduce the losses.

**Figure 1.** Luminescent solar concentrator.

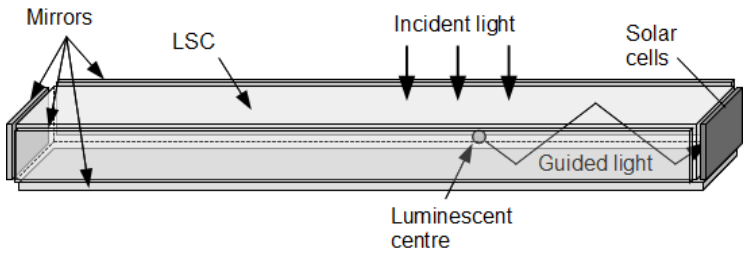


LSCs have several advantages over conventional geometric solar concentrators. LSCs can accept both direct and diffuse sunlight and indeed it is believed that LSCs can perform better under diffuse light than under direct light, so a sunlight tracking system is not necessary. The extended surface area of LSCs enables effective heat dissipation, hence avoiding the need for any cooling systems and allowing solar cells coupled at the edges to operate at the optimum temperature. In addition, LSCs can be used as building facades such as roofs, windows, walls or pavements. The electricity generated by LSC systems is consumed directly by electricity customers. Transmission of the solar electricity across electrical distribution systems can be avoided. As a result, power transmission losses can be reduced and technical issues caused by the integration of renewable energy sources with the distribution networks can be avoided [7–9].

To improve the radiation transfer of LSCs, computer modeling of LSCs becomes very essential as it can be used to determine the optimum design parameters of LSCs. Those parameters are the quantum efficiency of luminescent materials, concentration of luminescent materials, refractive index of the host, red-shift of the luminescent materials, thickness of LSCs, geometries of LSCs, diffuse or direct sunlight and surface contour of LSCs. Computer simulation of LSCs is required to fine-tune each of the parameters in order to achieve the maximum emission at the edge of LSCs.

Currently, there are two approaches of modeling LSCs, namely thermodynamic modeling [10] and ray-tracing modeling [11]. Thermodynamic modeling is a detailed balance model which is based on the radiative energy transfer between mesh points in the concentrator, whereas ray-tracing modeling is used to track every incoming photon and determine its fate [12]. Thermodynamic and tray-tracing

models have been used to simulate the performance of LSCs under direct sunlight conditions in order to optimize the performance of LSC with respect to the size of luminescent quantum dots, inclusion of mirrors and multi-layers of the LSC [10–14]. The accuracies of thermodynamic and ray-tracing models are about 4% and 11%, respectively.

Both thermodynamic and ray-trace modeling provide useful tools for optimizing the performance of a LSC and predicting the electrical output. Thermodynamic modeling can be easily used to simulate a simple rectangular LSC shape under direct sunlight. However, it is not flexible enough to model various geometries and the surface contours of LSCs under diffuse sunlight. Ray-tracing modeling is able to model various surface geometries of LSCs under direct and diffuse sunlight. However, this modeling requires a substantial amount of input measurement data from a case study. As described in [13,14], the ray-tracing modeling requires a collection of emission spectra from a luminescent material at various different excitation wavelengths in addition to the dimension, refractive index and extinction coefficient of LSC, quantum yield of dye, light source spectra and light intensity distribution. Also, the simulation time required by the ray-tracing method is enormous because forward ray-tracing is used to trace a large amount of photons from the source to their final destinations.

The objective of this research work was to study the performance of a LSC with various orientations under direct and diffuse sunlight conditions. The novelty of this hybrid model is the idea of integrating the thermodynamic model with the backward ray-tracing model. This model is a compromise tool that can off-set the weaknesses of the individual models. Therefore, it could be a fast, effective and powerful tool to simulate the performance of LSCs with various orientations under diffuse and direct sunlight. As a result, the technical and economical viability of using LSCs as building facades can be established.

In this hybrid algorithm, thermodynamic modeling is to calculate the luminescence at the edge of LSC due to the embedded luminescent materials. Then ray-tracing modeling is to determine the light intensity collected at the edge of LSC as a result of the unabsorbed portion of the incoming light. This ray-tracing modeling does not consider the emission of the luminescent materials in LSC. Therefore, the input data of the emission spectra at various different excitation wavelengths are not required in this hybrid algorithm. Furthermore, the simulation time required by the ray-tracing modeling is reduced substantially because this hybrid algorithm uses backward ray-tracing that only traces photons arriving at the target. As a result, this hybrid approach has the advantages of simplicity derived from the thermodynamic modeling which requires a minimum data input, and flexibility from the ray-tracing approach where different LSC surface geometries under direct and diffuse sunlight can be studied with reduced simulation effort.

In this article, the details of the hybrid simulation approach are presented. To verify the simulation approach, a LSC with the dimension of 10 cm (length) × 5 cm (width) × 0.5 cm (thick) was constructed using unsaturated polyester as the host matrix and Rhodamine 6G as the organic dye. This LSC was placed under a filtered LED light source. The absorption spectrum of the LSC was measured by a calibrated USB4000 spectrometer. The emission spectra were measured at the edge of the LSC. The simulation model of the LSC was developed using the hybrid algorithm. The simulated emission spectra were then generated and compared with the experimental spectra. The simulated results were in a good agreement with the experimental ones.

## 2. Description of the Hybrid Algorithm

### *2.1. Flow Chart of the Hybrid Algorithm*

In this hybrid simulation approach, the two-flux thermodynamic model as developed by the authors in [15] was modified and used in conjunction with an open source ray-tracing program, namely Radiance [16]. The input parameters required by the modified two-flux thermodynamic model are LSC dimensions, reflective index, luminescent dye concentration, absorption cross-section, luminescent quantum efficiency and temperature. Then the input parameters required by the ray-tracing program are light source radiation spectrum and profile, LSC dimensions, reflective index and absorption coefficient. The ray-tracing model simulates the average irradiation spectrum received by the photovoltaic cells, without considering the contribution from the dye emission. It also simulates the average irradiation spectrum as seen by the dye particles at the top surface of LSC, which is then passed to the thermodynamic model. The thermodynamic model simulates the average irradiation spectrum contributed by the dye emission. The average irradiation spectra from the two models are then combined to provide the overall irradiation output spectrum. This spectrum is considered as the incident light to the photovoltaic cells at the edge of LSC. Figure 2 is the flow chart of the simulation algorithm.

**Figure 2.** Hybrid simulation program flow chart.

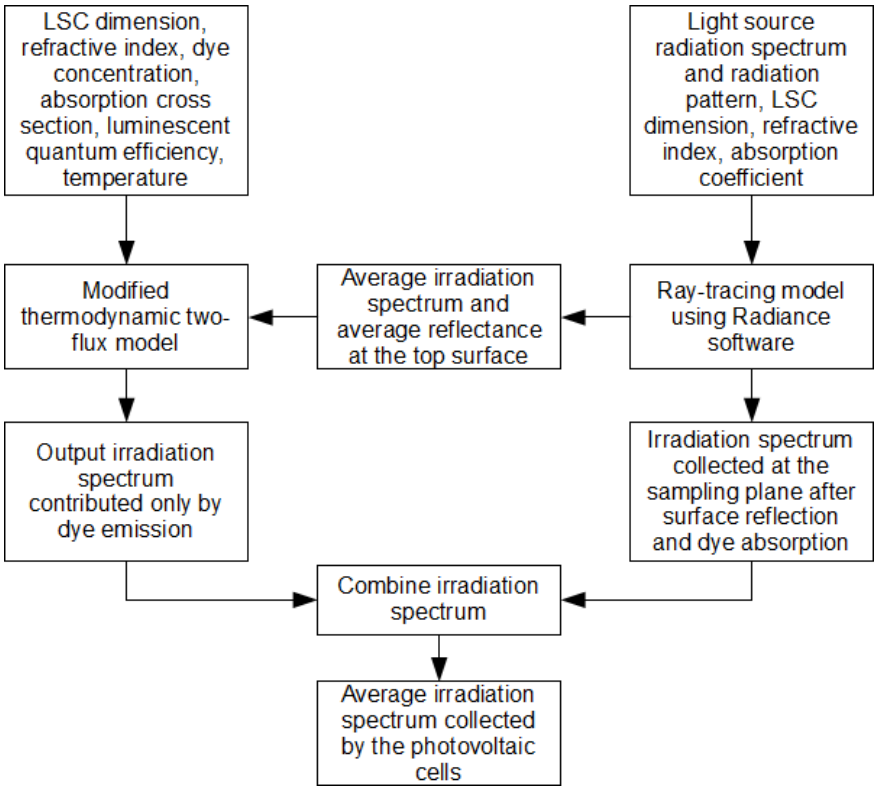

### *2.2. Ray-Tracing Model*

The open source ray-tracing program Radiance was used in the ray tracing model of the hybrid algorithm [17]. A ray travels from a light source to its final destination. Forward ray-tracing is a method that traces the ray from the light source to the final destination which is different from backward ray-tracing whereby the ray is traced backwards from the final destination to the light source.

The Radiance software uses the light-backward ray-tracing method to trace light from a point of interest into the scene and back to the light sources. Its built-in function "rtrace" can trace light from the point along a specific direction and output the radiant intensity for that direction. The unit of the radiant intensity is W $m^{-2}$ $sr^{-1}$. The total radiant intensity (irradiance) at the point is calculated by integrating all the light intensities arriving at that point from all the directions. The main objective of using Radiance is to determine the average irradiation across the edge of LSC where solar cells are attached to.

A Linux Shell script was written which executes the "rtrace" program in Radiance to perform the ray tracing. The program will then trace lights from a specific direction at a point with a particular wavelength each time the program is called.

The LSC model is created in a text file called scene description file where the wavelength dependent variables and the parameters of LSC are defined. Those wavelength dependent variables are incident light intensity, refractive index of the LSC and extinction coefficient of the LSC. The material properties, such as refractive index and extinction coefficient, are assumed to be constant along the *x*, *y* and *z* directions. The scene description file for a simple rectangular LSC structure as shown in Figure 3 is given in Figure 4. To include the absorption of the material in LSC, a mist type material is created on the LSC surfaces to model the dye's wavelength dependent absorption.

The software can handle both Lambertian and specular surfaces. All the mirror surfaces were modeled as specular surfaces. The reflections from the LSC surfaces are also specular reflections. All other reflective surfaces in the simulation case studies have the properties ranging between perfect Lambertian and perfect specular. The reflection model used in the software is physically based and the detail of this model can be found in [18].

**Figure 3.** Dimensions of the LSC used in the ray-tracing model.

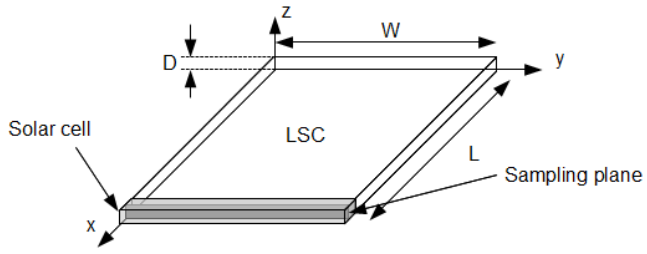


where:

*L* = Length of the LSC (m);

*W* = Width of the LSC (m);

*D* = Depth/thickness of the LSC (m).

**Figure 4.** Scene description file for the rectangle structure of LSC.

```
# scene description for LSC with arbitrary parameters.
# the red color ray is treated as monochromatic ray with a specific wavelength,
# therefore only red color parameters are defined.

# define a dielectric type surface with refractive index = 1.58.
void dielectric matrixmat
0
0
5 1 0 0 1.58 0

# create a box extending from the origin to (0.1,0.05,0.005) (in meters).
!genbox matrixmat lsc 0.1 0.05 0.005

# define a mist type material with extinction coefficient = 50, albedo = 0.
void mist lscmat
0
0
6 50 0 0 0 0 0

# create a box extending from the origin to (0.099998,0.049998,0.004998) (in meters).
# transform the box by translating it by 0.000001 to x-direction,
# then 0.000001 to y-direction, and 0.000001 to z-direction.
!genbox lscmat lscabs 0.099998 0.049998 0.004998 | xform -t 0.000001 0.000001 0.000001
```

Then the function "rtrace" is called to perform the ray tracing for each wavelength at a particular point of the sampling plane with all the directions. This is repeated for all the specified locations across the sampling plane and all wavelengths ranging from 300 to 800 nm. The irradiance values calculated for the specified locations on the sampling plane are then averaged over the total surface area to give the average irradiance output $E_{\text{average}}$. The discrete ordinate method used by Mishra *et al.* [15] is employed in the algorithm to determine the integration of radiance intensity with respect to solid angle over a hemisphere. The calculation details are shown in Appendix A. Figure 5 shows the algorithm for executing the ray tracing modeling. A maximum of 30 reflections are considered in the simulation case studies.

The output $E_{\text{average}}$ will be converted into photo flux by using the following equation:

$$\Phi_{\text{rtrace}}(\lambda) = E_{\text{average}}(\lambda)\frac{\lambda}{hc} \tag{1}$$

where:

$\Phi_{\text{rtrace}}(\lambda)$ = the average spectral photon flux from ray-tracing model (photons s $m^{-2}$ $nm^{-1}$);

$E_{\text{average}}(\lambda)$ = the average spectral irradiance (W $m^{-2}$ $nm^{-1}$);

$\lambda$ = Radiation wavelength (nm);

$c$ = Speed of light in free space (m $s^{-1}$);

$h$ = Planck constant (J s).

### *2.3. Thermodynamic Model*

The two-flux thermodynamic model [19,20] is used here. In this model, the radiation transfer equation is solved for the simplified case of infinite parallel plane. The dye emission is modeled by introducing the photon chemical potential (a function of position in the LSC) into the Planck's distribution function in the radiation transfer equation for an absorbing, emitting, non-scattering medium.

**Figure 5.** Flow chart of the ray-tracing model.

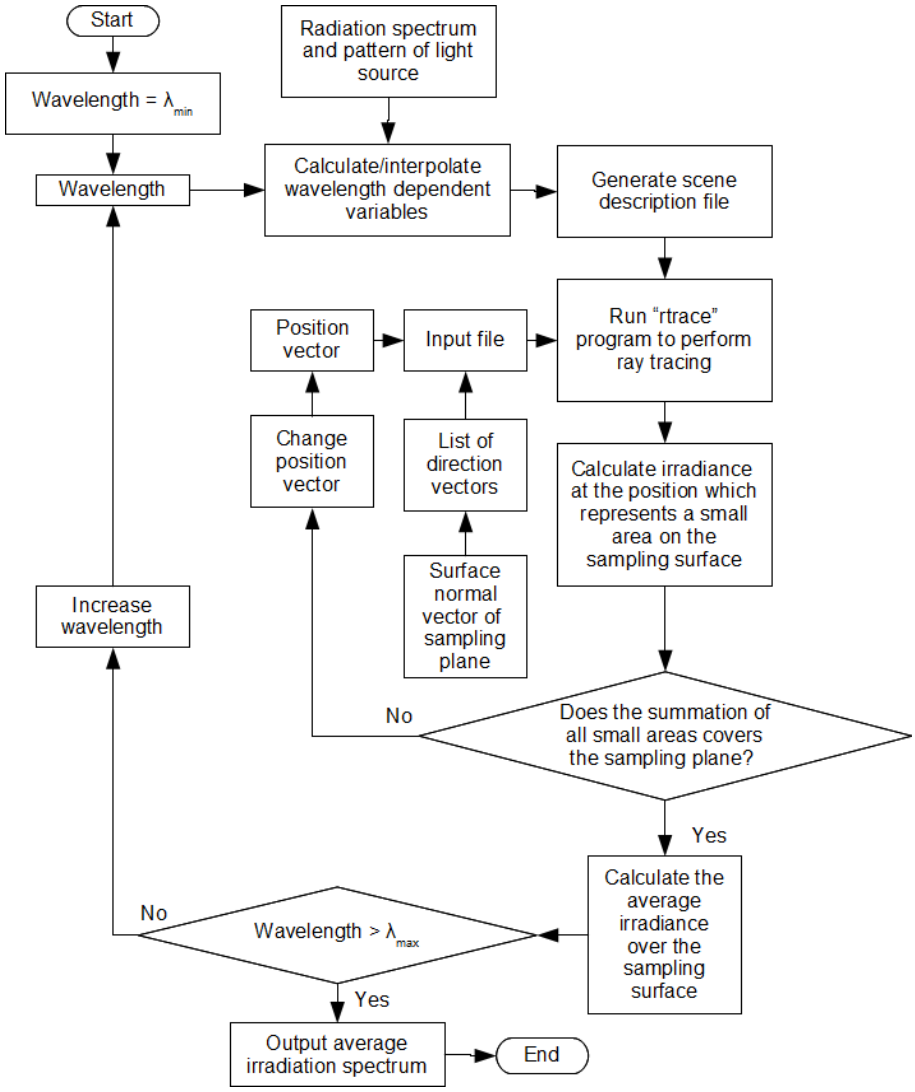


The radiative transfer equation is the fundamental description of the variation of radiation intensity in a medium in response to the absorption and emission of the medium [21]. The solution of the radiation transfer equation together with the equation specifying the principle of detailed balance as shown in Equation (2), form a set of simultaneous equations which cannot be solved analytically. However numerical solution can be obtained using Newton's method.

The principle of detailed balance is given by:

$$\int \sigma_e(v)[I_E + I_T]dv = \int \frac{\sigma_e(v)}{Q_e} B(v)dv \quad (2)$$

where:

$v$ = Radiation frequency (Hz);

$\sigma_e$ = Absorption cross section of dye ($m^2$);

$Q_e$ = Luminescent quantum efficiency;

$B$ = Luminescent brightness (photons $s^{-1}$ $m^{-2}$ $Hz^{-1}$);

$I_E$ = Escaped flux (photons $s^{-1}$ $m^{-2}$ $Hz^{-1}$);

$I_T$ = Trapped flux (photons $s^{-1}$ $m^{-2}$ $Hz^{-1}$).

The left hand side of Equation (2) states that the total number of photons contributes to the net upward transition rate of electrons in the dye particles, which is calculated by multiplying the total photon flux received by the dye particles with the absorption cross section of the dye particles.

The right hand side of Equation (2) states that the total number of emitting photons divided by the luminescent quantum efficiency contributes to the net downward transition rate of electrons in the dye particles. The total number of emitting photons is calculated by multiplying the luminescent brightness of the dye particles with the absorption cross section of the dye particles. Equation (2) concludes that the net upward transition rate is equal to the net downward transition rate in the dye particles.

A flux emitting from the LSC dye can escape to the atmosphere or bounce back from the air to the LSC boundary, depending on whether the existing flux is within the optical escape cone or not. If the existing flux is within the escape cone, then the flux escapes to the atmosphere. The escaped flux is the average photon flux escaping to the atmosphere. The trapped flux is the average photon flux being trapped inside the LSC, as illustrated in Figure 6.

**Figure 6.** Escaped flux and trapped flux.

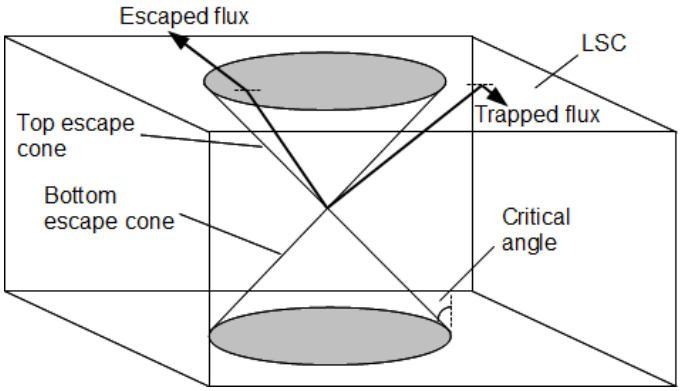


The dye emission is modeled by introducing photon chemical potential in Equation (3):

$$B(v) = \frac{8\pi n^2 v^2}{c^2} \frac{1}{e^{[hv-\mu]\beta} - 1} \tag{3}$$

where:

$\mu$ = Photon chemical potential (J);

$\beta$ = 1/kT ($J^{-1}$);

$k$ = Boltzmann constant (J $K^{-1}$);

$T$ = Temperature (K);

$q$ = Elementary charge constant (C).

The thermodynamic two-flux model introduced by Chatten *et al.* [19] is used to perform the simulation of dye emission in one dimension. The horizontal flux propagating toward the edge is calculated using the solution of horizontal flux in 3D thermodynamic model [20]. In this model, it was assumed that the photon flux escaped from the horizontal surfaces is negligible as compared to the escaped flux from the top and bottom surfaces, so a two-flux model was used instead of the complete 3D model to reduce the simulation time. Calculation details of two-flux model for dye emission and that of horizontal flux are outlined in Appendix B. Equations (2) and (3), together with Equations (B.1)

and (B.2) are used to solve the photon chemical potential numerically using Newton's method. Equation (B.16) is used to calculate the horizontal escaped flux from the edge as represented by $\Phi_{\text{thermo}}(\lambda)$. Figure 7 shows the flow chart of the thermodynamic modeling. The material parameters are assumed to be constant along the *z*-direction.

**Figure 7.** Flow chart of the thermodynamic model.

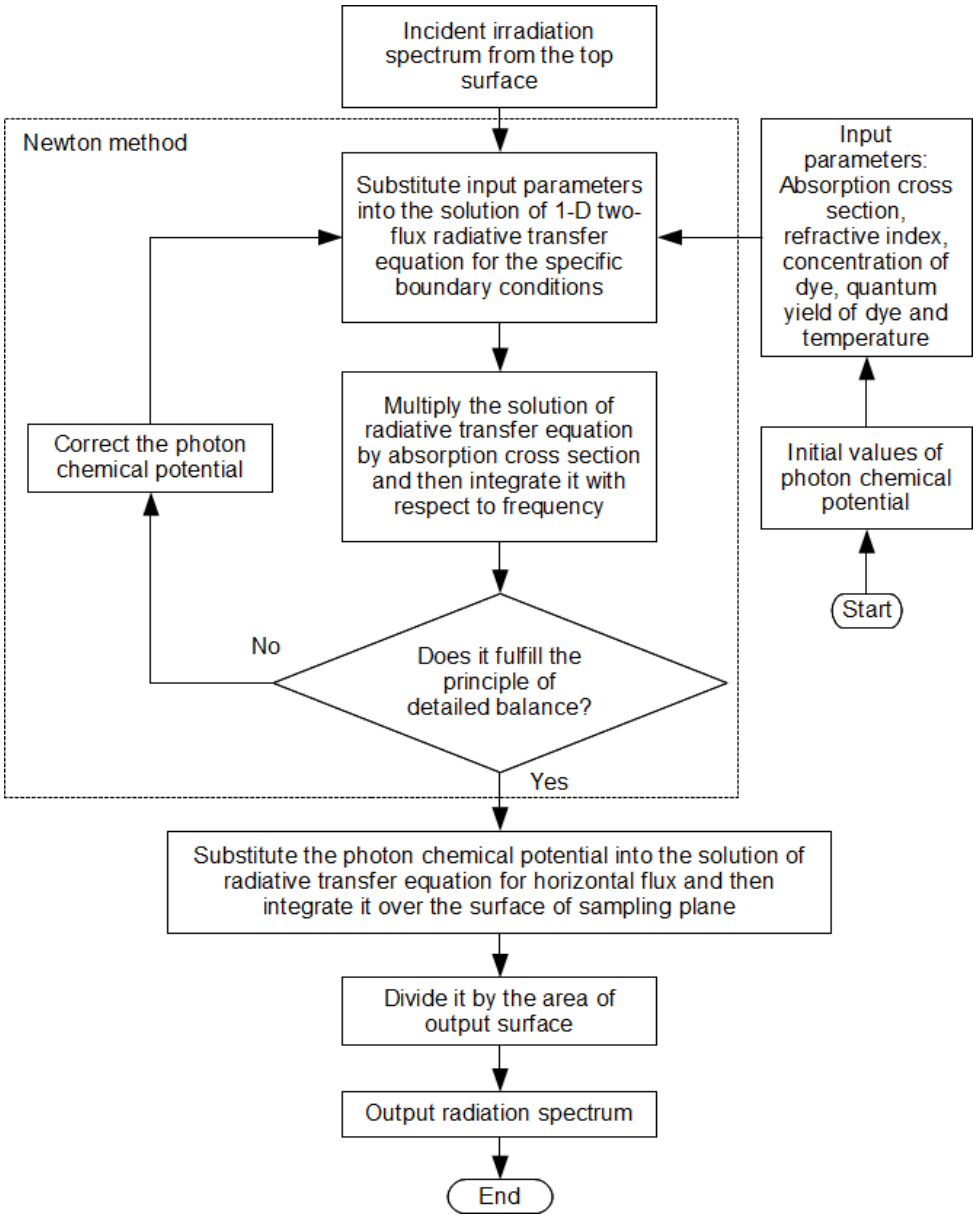


The photon chemical potential is one of the parameters used in the thermodynamic model to determine the dye emission [19], therefore it is dependent on the *x*, *y* and *z* directions. However, due to the uniform incident light distribution across the LSC's top surface, the dye emission is constant along the *x* and *y* directions, and varies only along *z* direction and therefore, the photon chemical potential is a function of the *z* direction only.

To date, a correlation between the photon chemical potential and the material parameters is not apparent from any literature, therefore, it was assumed that the material parameters are constant,

regardless of the chemical potential. The iterative correction of photon chemical potential does not affect the input material parameters in the simulation model.

The total photon flux is the summation of photon flux from ray tracing model and photon flux from thermodynamic model as given below:

$$\Phi(\lambda) = \Phi_{\text{rtrace}}(\lambda) + \Phi_{\text{thermo}}(\lambda) \tag{4}$$

## 3. Experiment Setup

The LSC sample used in the experiment is a 10 cm × 5 cm × 0.5 cm unsaturated polyester (UP) with 5% methyl methacrylate (MMA) doped with $3.75 \times 10^{-5}$ M Rhodamine 6G. The preparation steps of the LSC sample were described in [21].

The experiment setup is shown in Figure 8. A white light emitting diode (LED) from a torch light was used as the light source, filtered by a blue optical filter which consists of six layers of blue transparent plastic film. The filtered light source illuminated the LSC sample from a point at 5 cm above the center of the LSC sample. Mirrors were put at the bottom and three edges, except for the edge where the irradiance output was collected by a cosine corrector which was connected to a wavelength-and-radiometry-calibrated Avantes Spectrometer via an optical fiber. The reflective surfaces of the mirrors were covered by black paper, except for the part in contact with the LSC sample.

**Figure 8.** Experiment setup.

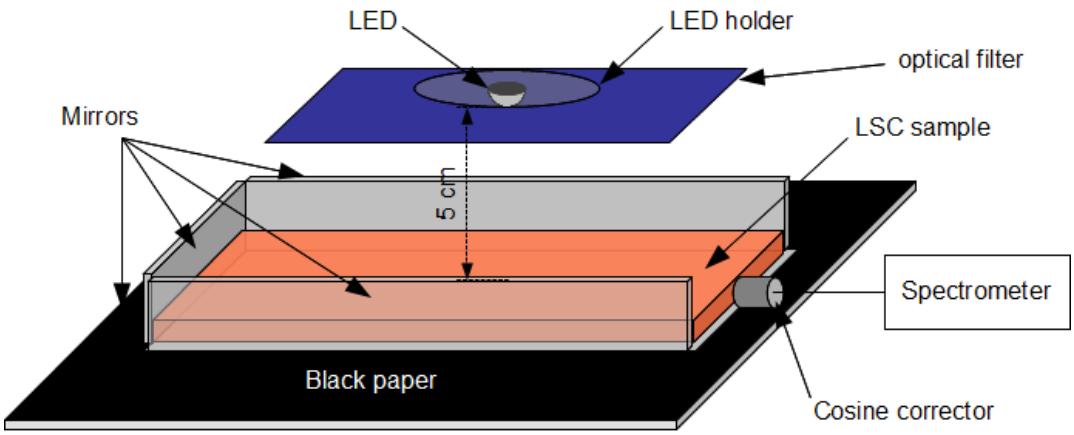


## 4. Simulation of the Experimental Setup

The purpose of the experiment is to verify the solution obtained from the proposed simulation approach. Therefore the program was modified to introduce the effect of cosine corrector and the small air gap between the LSC edge surface and the cosine corrector diffuser surface. The cosine corrector was modeled as a perfect diffuser collecting light from a 180 degree field of view. The simulation input parameters are listed in Table 1, together with the corresponding measured values.

**Table 1.** Simulation input parameters *versus* the actual measured values.

| Property | Simulation Input Parameter | Measured Value/Spectrum |
|---|---|---|
| Dimension | 10 cm × 5 cm × 0.5 cm | 9.8 cm × 4.9 cm × 0.5 cm |
| Refractive index | 1.58 | 1.57 |
| Luminescent quantum efficiency | 0.95 [1] | Not measured. |
| Concentration | $3.75 \times 10^{-5}$ mol/dm$^3$ | $3.75 \times 10^{-5}$ mol/dm$^3$ |
| Temperature | 25 °C | Not measured |
| Absorption cross section (dye) | Refer to Figure 9 | Refer to Figure 9 |
| Absorption cross section (sample) | Refer to Figure 10 | Refer to Figure 10 |
| Incident light | Refer to Figure 13 | Refer to Figure 13 |

[1] Obtained from [23].

The absorption cross-section of the dye (Rhodamine 6G) was measured from a mixture of UP resin, Rhodamine 6G and MMA in the same proportion as in the hardened LSC sample. The mixture was put inside a 1 cm cuvette, with the mixture of UP resin and MMA as the reference solution. The absorbance was measured using a wavelength-calibrated Ocean Optics USB4000 spectrometer connected to the Ocean Optics CUV-ALL-UV cuvette holder, with the Mikropack HL-2000-HP-FHSA halogen light source connected to the cuvette holder at the opposite direction. The absorbance spectrum was then converted to absorption cross section spectrum, as shown in Figure 9.

**Figure 9.** Dye absorption cross section.

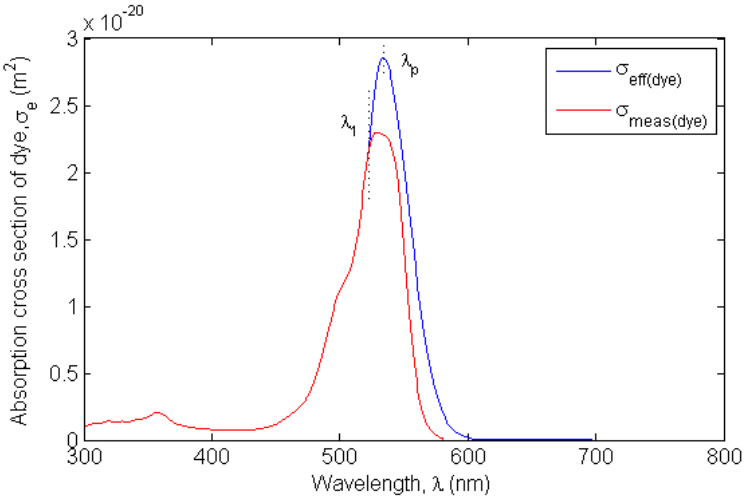


The absorbance of the sample was measured by fixing the solid LSC sample vertically in between two Ocean-Optics-84-UV-25 collimating lens mounted on an optical table. The Mikropack HL-2000-HP-FHSA halogen light source was connected to one of the collimating lens, while another lens was connected to the Ocean Optics USB4000 spectrometer. No reference sample was prepared in this case since there was some difficulty in preparing an ideal well-polished flat plate sample of 5 mm thickness for spectroscopic measurement. Therefore the reflection at the air-to-LSC boundary was ignored in the measurement. The absorbance spectrum was then converted to absorption cross section spectrum, as shown in Figure 10.

**Figure 10.** Sample absorption cross section.

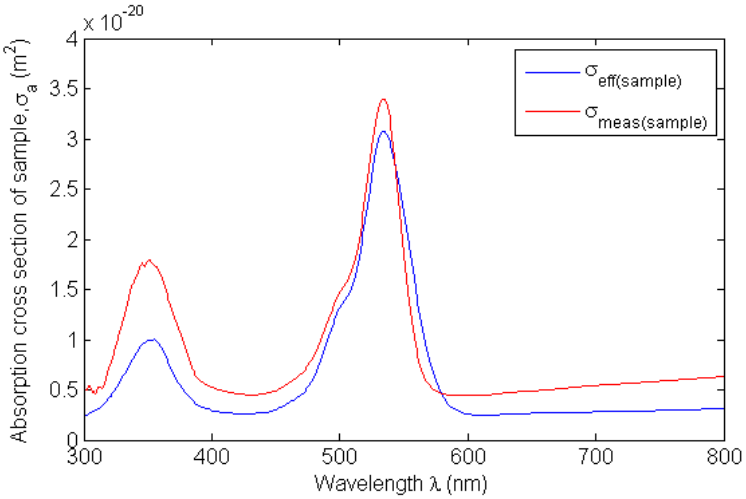


The red lines in Figure 9 and Figure 10 represent the experimental data, which is not the pure absorption cross sections of the dye and LSC plate because the data contains some unwanted effects such as the reflectance and absorption of the cuvette, reflectance of the LSC surfaces and emission of the dye. As a result, the experimental data could not be used directly as the input data to the simulation model. Attempts were carried out to remove all the distortions from the measurement data by using analytical approach. In these attempts, all the distortions were measured and fed into the analytical equations in the hope that the effective absorption cross sections of the dyes and LSC plate could be determined. However, it was found that none of the analytical equations took into account all the unwanted effects correctly. In fact, the analytical equations became relatively complicated in the situation where the top and bottom surfaces of LSC were not perfectly uniform and flat. Therefore, it was decided to use empirical approach to determine the effective absorption cross sections of the dye and LSC plate. Figure 11 describes the empirical approach used to find the effective absorption cross section of the dye. This absorption cross section spectrum, $\sigma_{meas(dye)}$, is used as the initial spectrum to be curve fitted. A Gaussian function and a cubic spline function are used to curve fit $\sigma_{meas(dye)}$. The result of the curve fitting $\sigma_{fit\_ini(dye)}$ is fed into the thermodynamic model to generate an emission spectrum with a peak wavelength of $\lambda_{em\_peak(sim)}$. It is noticed that the absorption cross section spectrum of the dye affects predominantly the wavelength of the peak. Therefore, $\lambda_{em\_peak(sim)}$ is used to compare with peak wavelength in measured emission spectrum $\lambda_{em\_peak(meas)}$. The difference between the two is used to adjust a constant, $C_1$. This new constant value is used in the Gaussian function in $\sigma_{fit(dye)}$ to produce a new absorption cross section spectrum which in turn is fed into the thermodynamic model. This adjustment process is repeated until the difference between $\lambda_{em\_peak(meas)}$ and $\lambda_{em\_peak(sim)}$ is less than a specified tolerance. The effective absorption cross section of the dye, $\sigma_{eff(dye)}$, is then determined.

Figure 12 describes the empirical approach used to find the effective absorption cross section of the LSC sample, $\sigma_{eff(sample)}$. LSC sample means the host material with the dye. Firstly, the absorption cross section of the host material without the dye, $\sigma_{meas(host)}$, is determined by subtracting the measured absorption cross section of the LSC sample, $\sigma_{meas(sample)}$, from that of the dye, $\sigma_{meas(dye)}$.

**Figure 11.** Flow chart for calculating the effective absorption cross section of the dye.

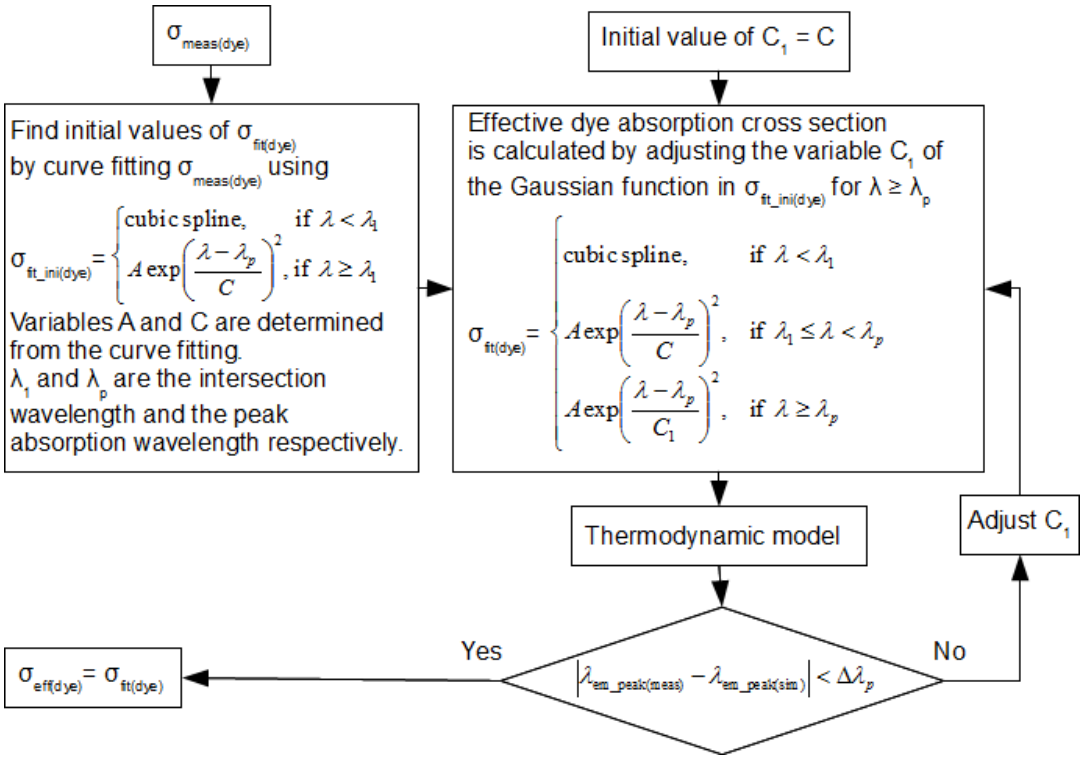


**Figure 12.** Flow chart for calculating the effective absorption cross section of the sample.

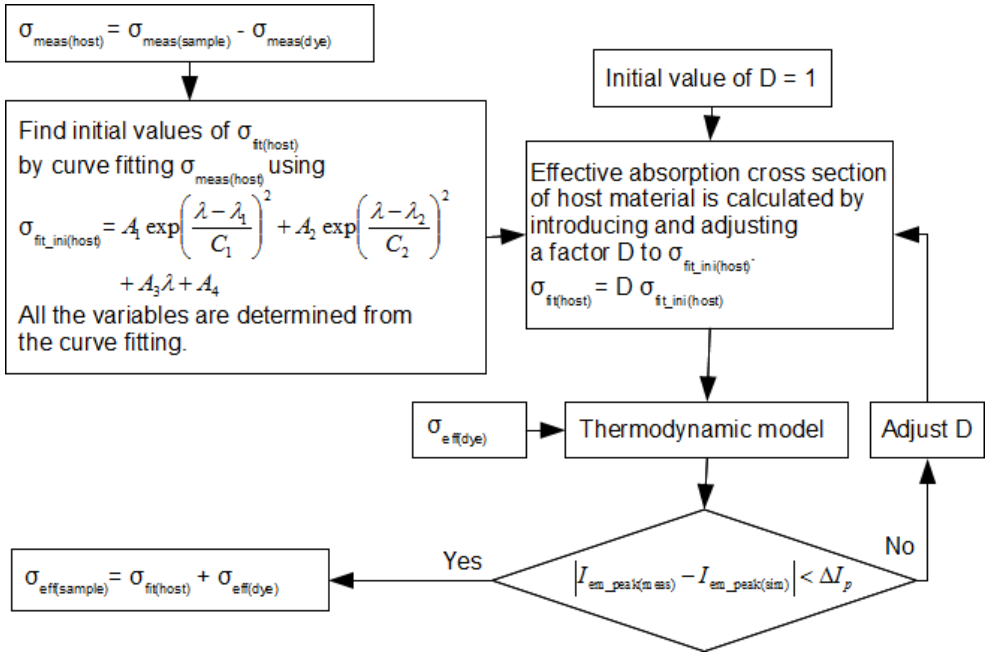


A combination of linear and Gaussian functions was used to curve fit $\sigma_{meas(host)}$ in order to generate a function, $\sigma_{fit\_ini(host)}$. The magnitude of the function, $\sigma_{fit\_ini(host)}$, is then multiplied by a factor $D$, in order to correct the effect of the imperfection on the surface of the solid LSC sample. The factor $D$ is always less than one. Then the corrected function, $\sigma_{fit(host)}$, and the effective absorption cross section of the dye, $\sigma_{eff(dye)}$, are fed into thermodynamic model to generate the emission spectrum. It is noticed that the

absorption cross section spectrum of the host material mainly affects the magnitude of the peak. Therefore, the magnitude of the peak in the emission spectrum, $I_{em\_peak(sim)}$, is used to compare with the measured peak magnitude, $I_{em\_peak(meas)}$. The difference between the two is used to adjust the factor $D$, which in turn is used in Gaussian functions to generate a new function. The adjustment process is repeated until the difference ($I_{em\_peak(meas)} - I_{em\_peak(sim)}$) is less than a specified tolerance. The effective absorption cross section of LSC sample, $\sigma_{eff(sample)}$, is then determined.

The effective absorption cross sections of the dye and the sample are represented by the blue lines in Figures 9 and 10. These effective absorption cross sections of the dye and the sample were used in various case studies with different LSC settings. The simulation results generated from one setting were found to match well with the experimental results from the same setting. This is how the effective absorption cross section of the dye and the sample were verified.

There are two peaks in Figure 10. The peak at the wavelength of 350 nm is the absorption cross section of the host material or unsaturated polyester without considering the dye. The peak at wavelength of 530 nm is the absorption cross section of the dye. It can be noticed that the peak at wavelength of 530 nm is the same as that in Figure 9. The peak at 530 nm is higher than that at 350 nm because the host material itself is more transparent than the dye.

The incident light source irradiance spectrum as shown in Figure 13 was measured using the Avantes spectrometer connected to a cosine corrector via an optical fiber, by pointing the cosine corrector upward to the center of the LED after the optical filter, at a distance of 5 cm from the LED. The LED and the optical filter was lumped together and modeled as a round shape isotropic area source having a diameter of 3 mm and radiance value of $L_{FilteredLED}$ calculated using Equation (5) in the Radiance scene description:

$$L_{FilteredLED}(\lambda) = E_{measured}(\lambda) \Big/ \left[ \pi \sin^2 \left( \tan^{-1} \frac{d/2}{D} \right) \right] \tag{5}$$

where:

$E_{measured}$ = Measured incident light spectrum;

$d$ = Diameter of the LED (0.3 cm);

$D$ = Distance between the sample and the light source (5 cm).

The incident light spectrum was sampled in Radiance by generating a scene that consists of the light source only, representing the experiment setup which measures the incident light irradiance spectrum. The irradiance collected by the vertically upward sampling plane over a hemisphere at a point 5 cm below the light source is obtained using the calculation in Appendix A. The minimum values of $M_\theta$ and $M_\varphi$ were determined by increasing their values gradually until the sampled spectrum matches the measured incident irradiance spectrum reasonably well. The sampled spectrum as shown in Figure 13 is used as the input parameter in the thermodynamic model. For this experiment, the average reflectance at the top surface of LSC was calculated using Equation (B.12) from Appendix B, since it was assumed that the top surface of the LSC sample in the experiment is a perfectly flat surface where the average reflectance can be easily calculated.

**Figure 13.** Incident light spectrum.

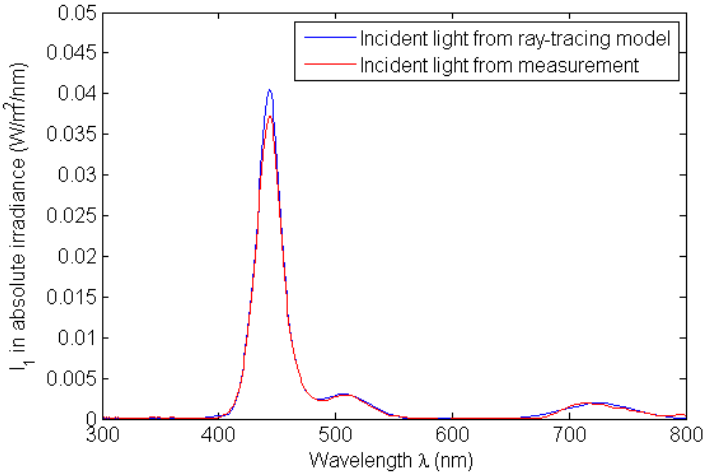


The scene description file used by the ray-tracing model created by the Shell script model the scene set up which is shown in Figures 14 and 15. The dimension in the scene was determined from the actual experiment setup. The tilt angle of the sampling plane was due to the structure of the connector connecting the optical fiber and the cosine corrector, which has a diameter slightly larger than the diameter of the cosine corrector, and causes a small tilt when the cosine corrector was put on the flat surface.

**Figure 14.** Ray-tracing simulation model.

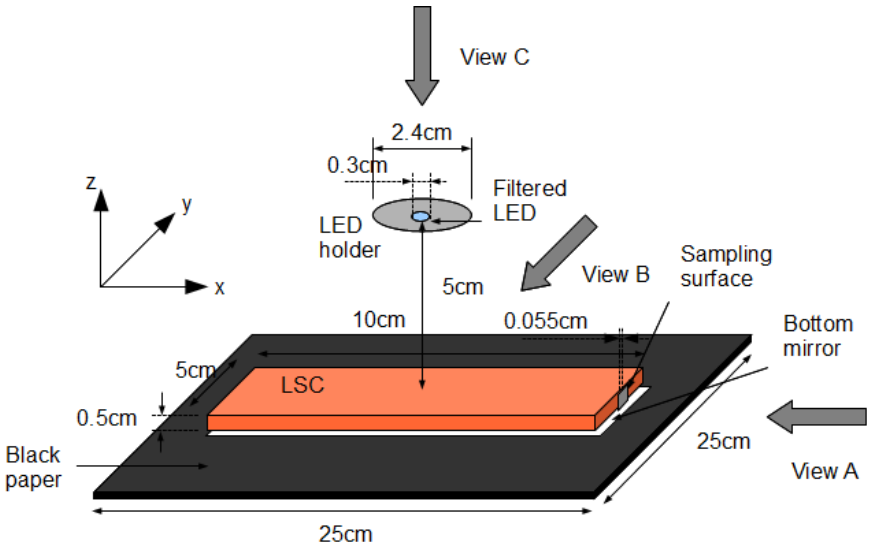


The filter holder surface was included to account for the small reflection from that surface, which was collected by the cosine corrector directly. The black paper was modeled as a plastic type surface having reflectance of 0.05, specularity fraction of 0.1 and roughness of 0.15. The LSC was modeled by a combination of dielectric surfaces with the specified refractive index and the mist type material to account for the absorption. A 2 mm dielectric with refractive index of 1.52 was included for the bottom mirror to model the thin layer of glass on the mirror used in the experiment. The mirrors at the 3 edges were modeled by metal type surface with reflectance of 1, specularity of 1 and zero roughness.

**Figure 15.** Two-dimensional view of the ray-tracing simulation model.

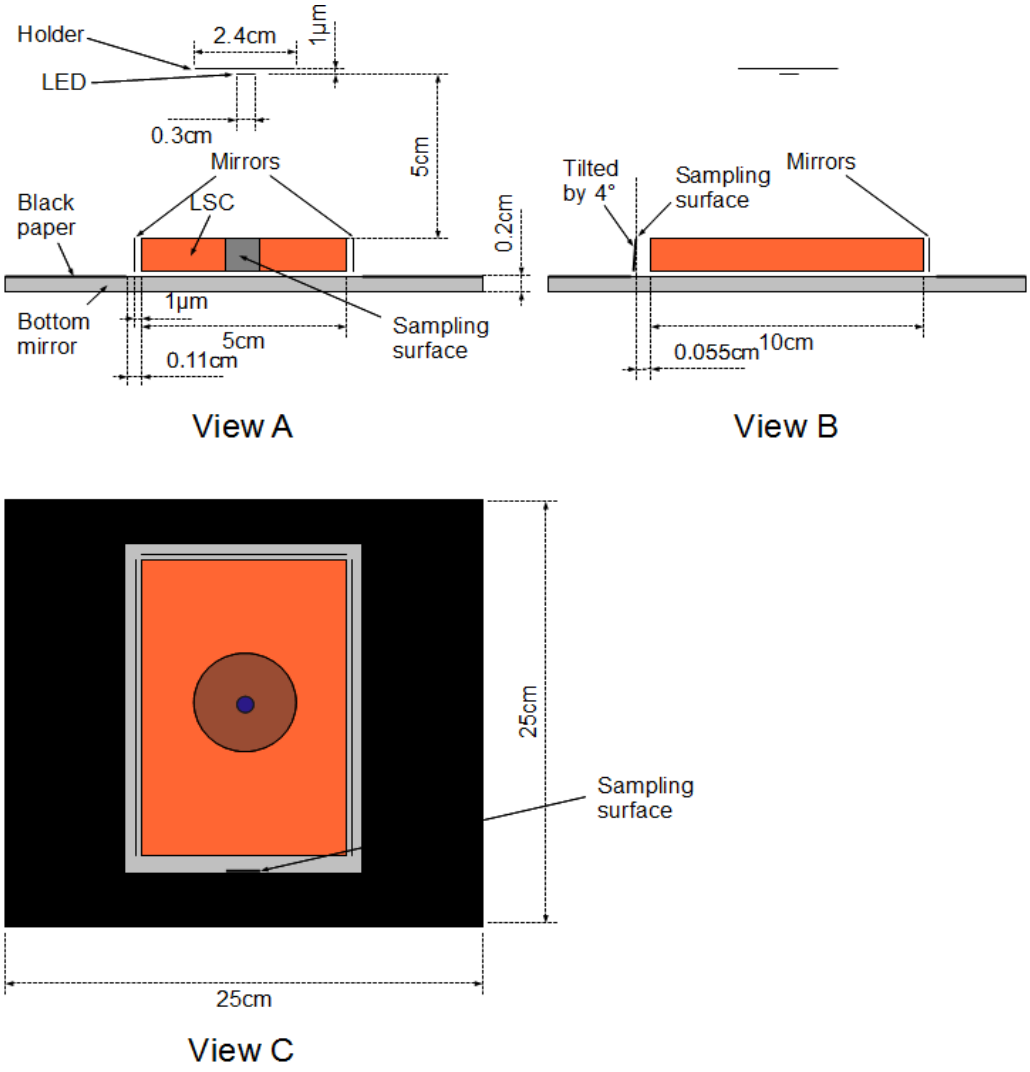


## 5. Results and Discussion

The measurement result is shown in Figure 16, together with its magnified graph in the middle. Incident light was attenuated by the optical filter in the region of wavelength between 550 nm to 650 nm so that the dye emission can be clearly observed in the measured emission spectrum from the edge.

The emission spectrum in Figure 16 represents both luminescent emission plus light confinement. Since theoretically the separate components come from splitting the solution of radiative transfer equation into two parts where one part is affected by the incident light only, and another part affected by the dye emission. Therefore, it is not possible to separate them in real measurement and verify each contribution separately.

**Figure 16.** Experimental measurement result.

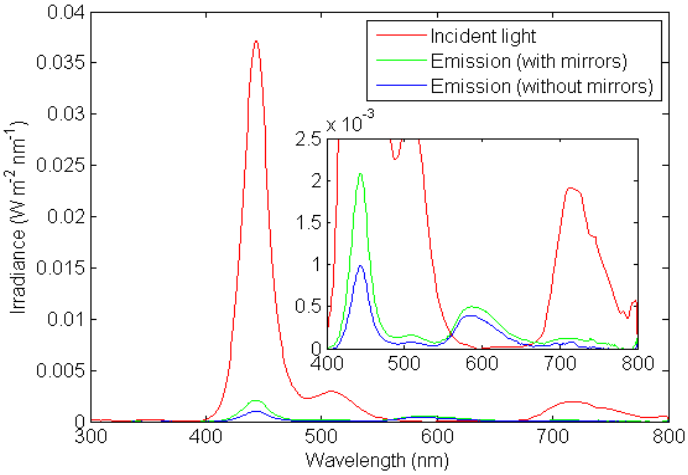


The simulation results for the cases of LSC with mirrors and without any mirror are shown in Figures 17 and Figure 18 respectively, together with the experimental result for comparison. Two peaks were observed in the experimental result.

**Figure 17.** Simulation result *versus* experimental result for the case with mirrors.

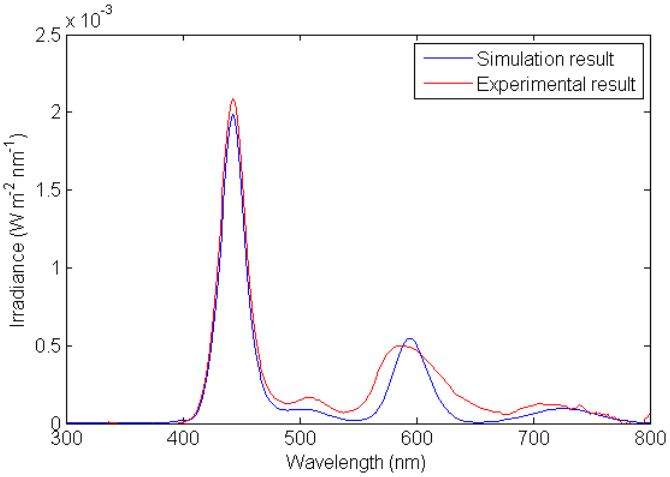


**Figure 18.** Simulation result *versus* experimental result for the case without any mirror.

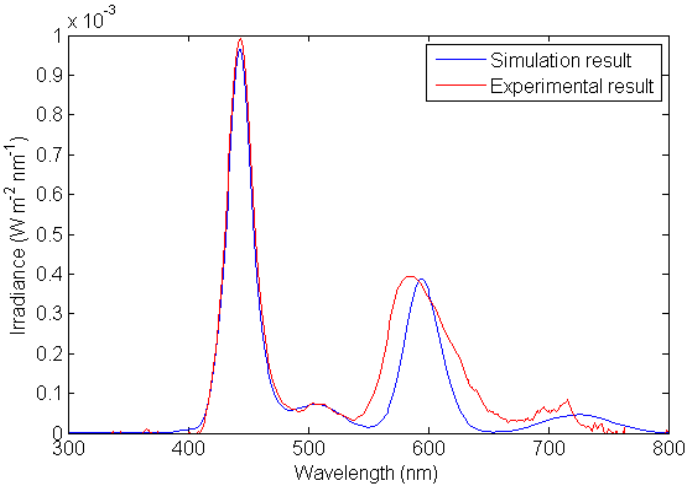

The separate contributions from each model are shown in Figures 19 and Figure 20. The irradiance values of the peaks and the corresponding wavelengths are listed in Table 2, together with the calculated values from simulation result. The simulation output can predict the peak irradiance and wavelength in the measurement result for the case without any mirror accurately using the same set of parameters adjusted to match the measurement result for the case with mirrors. Therefore it validates the adjustment of parameters described in Section 4.

Two peaks are observed from the output irradiance spectral of LSC. The first peak at 443 nm is contributed by the trapped light. The second peak at 594 nm is from the luminescence of the dye. The first peak is much higher than the second peak. The surface of LSC is able to capture the incident light and guide the light to the edge. The contribution of the trapped light to the output irradiance of LSC is significant. Therefore, it is important to consider the contribution of the trapped light into the design of LSC.

**Figure 19.** Separate contribution from the two models for no-mirror case.

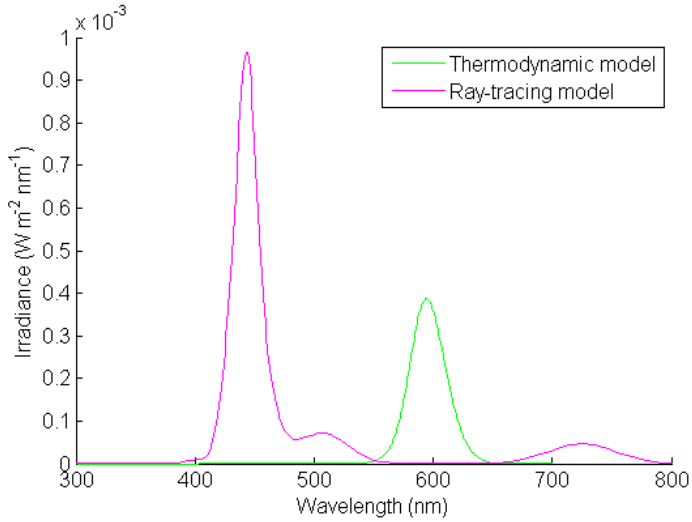


**Figure 20.** Separate contribution from the two models for with-mirror case.

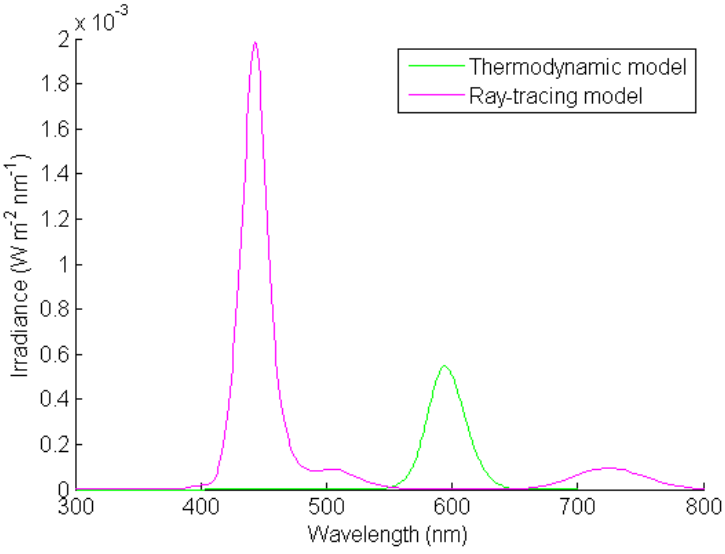

**Table 2.** Peak irradiance and wavelength in irradiance spectrum.

| Peak in Irradiance Spectrum | Simulation | | Experiment | |
|---|---|---|---|---|
| | Irradiance ($W/m^2/nm$) | Wavelength (nm) | Irradiance ($W/m^2/nm$) | Wavelength (nm) |
| 1st peak, with mirrors | $1.99 \times 10^{-3}$ | 443 | $2.09 \times 10^{-3}$ | 443 |
| 1st peak, without mirrors | $9.66 \times 10^{-3}$ | 443 | $9.92 \times 10^{-3}$ | 444 |
| 2nd peak, with mirror | $5.48 \times 10^{-4}$ | 594 | $5.02 \times 10^{-4}$ | 586 |
| 2nd peak, without mirror | $3.89 \times 10^{-4}$ | 594 | $3.89 \times 10^{-4}$ | 588 |

Total irradiance in Table 3 is calculated by integrating the irradiance spectrum with respect to the wavelength. The differences between the predicted total irradiance values from simulation and the measured values are 22% for the case with mirrors, and 16% for the case without any mirror.

**Table 3.** Comparison of total irradiance from simulation result and experimental result.

| Total Irradiance | Simulation ($W/m^2$) | Experiment ($W/m^2$) | % Difference |
|---|---|---|---|
| With mirrors | 0.0872 | 0.1125 | 22% |
| Without mirrors | 0.0489 | 0.0579 | 16% |

The reasons of the mismatch between the simulation output and the experimental measurement include the scattering effect which occurs in the transparent host material and the difficulties to model the non-perfectly-flat LSC surfaces correctly.

In the simulation cases studies, the reflectors at the bottom and edges of LSC are specular reflector, however the hybrid model can also be used for diffuse reflectors as long as the effective reflectance of the diffuse reflectors is first modeled using ray-tracing. The thermodynamic and ray-tracing models can handle various values of effective reflectance of the diffuse reflectors. This study on this effect can contribute to a second publication.

## 6. Conclusions

A new hybrid simulation approach is developed based on a combination of thermodynamic and ray-tracing modeling. This hybrid approach has the ability to study the transfer of energy across a LSC with different surface geometries under direct and diffuse sunlight with minimum data input and reduced simulation efforts. To verify the simulation approach, unsaturated polyester and Rhodamine 6G were used to construct a LSC with dimensions of 10 cm (length) × 5 cm (width) × 0.5 cm (thick). This LSC was placed under a solar simulator. Several input parameters such as absorption cross section of the dye, absorption cross section of the host material and incident light were measured and fed into the simulation program.

The irradiance spectrum produced by the hybrid simulation approach is able to accurately predict the peak irradiance and the corresponding wavelength to be received at the edge of LSC. The spectrum output from the simulation can be used as the input parameter for photovoltaic cell simulation model for a more accurate analysis on the performance of the photovoltaic cells attached to LSC. Therefore this hybrid simulation approach is suitable to study the performance of photovoltaic cells attached to LSCs with different surface geometries under various sunlight conditions.

A hybrid LSC simulation model was developed using the idea of combining the thermodynamic and Radiance ray-tracing simulation models. The thermodynamic model has been well-developed. The ray-tracing simulation model is well-established free software. It can simulate various scenarios accurately, taking into account the effect such as the diffuse inter-reflection between building walls and physically based reflection model. Therefore, the development of the hybrid simulation model did not require any extensive modification and improvement on the programming code of the ray-tracing and thermodynamic models. This hybrid model can be a fast, powerful and cost-effective tool for the design of LSCs for building facades.

The hybrid model was used to carry out two case studies. The first case study was to determine the output irradiance of LSC with mirrors attached to the edges and bottom of LSC. The second case study was the one without mirrors. The output irradiance of LSC with mirrors was about 2 times higher than that without mirrors. The simulation results showed that the trapped light contributed significantly to the output of LSC. The accuracy of the hybrid model is about 18% as compared to the measurements. The possible reasons for the mismatch between the simulation output and the experimental measurement are the ray scattering effect which occurs in the transparent host material and the non-perfectly-flat surfaces of LSC.

The immediate tasks to be carried out will be to incorporate the ray scattering effect into the hybrid simulation model, to study the electrical performance of solar cells attached to the LSC and finally to investigate the effect of replacing the specular reflector at the LSC bottom by diffuse and Lambertian reflector.

## Acknowledgements

The authors would like to thank Ministry of Science Technology and Innovation in Malaysia for financial support.

## References

1. Rowan, B.C.; Wilson, L.R.; Richards, B.S. Advanced material concepts for luminescent solar concentrators. *IEEE J. Sel. Top. Quantum Electron.* **2008**, *14*, 1312–1322.
2. Barnham, K.; Marques, J.L.; Hassard, J.; O'Brien, P. Quantum-dot concentrator and thermodynamic model for the global redshift. *Appl. Phys. Lett.* **2000**, *76*, 1197–1199.
3. Werts, M.H.V.; Hofstraat, J.W.; Geurts, F.A.J.; Verhoeven, J.W. Fluorescein and eosin as sensitizing chromophores in near-infrared luminescent ytterbium(III), neodymium(III) and erbium(III) chelates. *Chem. Phys. Lett.* **1997**, *276*, 196–201.
4. Sholin, V.; Olson, J.D.; Carter, S.A. Semiconducting polymers and quantum dots in luminescent solar concentrators for solar energy harvesting. *J. Appl. Phys.* **2007**, *101*, 123114.
5. Rau, U.; Einsele, F.; Glaeser, G.C. Efficiency limits of photovoltaic fluorescent collectors. *Appl. Phys. Lett.* **2005**, *87*, 171101.
6. Debije, M.G.; Broer, D.J.; Bastiaansen, C.W.M. Effect of dye alignment on the output of a luminescent solar concentrator. In Proceedings of the 22nd European Photovoltaic Solar Energy Conference Exhibition, Milan, Italy, 3–7 September 2007; pp. 87–89.

7. Trichakis, P.; Taylor, P.C.; Lyons, P.F.; Hair R. Predicting the technical impacts of high levels of small scale embedded generators on low voltage networks. *IET Renew. Power Gener.* **2008**, *2*, 249–262.
8. Cipcigan, L.M.; Taylor, P.C. Investigation of the reverse power flow requirements of high penetrations of small-scale embedded generation. *IET Renew. Power Gener.* **2007**, *1*, 160–166.
9. Stannard, N.; Bumby, J.R.; Taylor, P.C.; Cipcigan, L.M. AC and DC aggregation effects of small-scale wind generators. *IET Renew. Power Gener.* **2007**, *1*, 123–130.
10. Chatten, A.J.; Farrell, D.J.; Buxton, B.F.; Büchtemann, A.; Barnham, K.W.J. Thermodynamic modelling of luminescent solar concentrators and modules. In Proceedings of the 21st European Photovoltaic Solar Energy Conference, Dresden, Germany, 4–8 September 2006; pp. 315–319.
11. Gallagher, S.J.; Eames, P.C.; Norton, B. Quantum dot solar concentrator behaviour, predicted using a ray trace approach. *Int. J. Ambient Energy* **2004**, *25*, 47–56.
12. van Sark, W.G.; Barnham, K.W.; Slooff, L.H.; Chatten, A.J.; Büchtemann, A.; Meyer, A.; McCormack, S.J.; Koole, R.; Farrell, D.J.; Bose, R.; *et al.* Luminescent solar concentrators—A review of recent results. *Opt. Express* **2008**, *16*, 21773–21792.
13. Schüler, A.; Kostro, A.; Galande, C.; Valle del Olmo, M.; de Chambrier, E.; Huriet, B. Principles of Monte-Carlo ray-tracing simulations of quantum dot solar concentrators. In Proceedings of ISES World Congress, Beijing, China, 18 September 2007; pp. 1033–1037.
14. Kostro, A.; Huriet, B., Schüler, A. PhotonSim: developing and testing a Monte-Carlo ray-tracing software for the simulation of planar luminescent solar concentrators. In Proceedings of the CISBAT 2007 International Conference, Lausanne, Switzerland, 4–5 September 2007.
15. Mishra, S.C.; Roy, H.K.; Misra, N. Discrete ordinate method with a new and simple quadrature scheme. *J. Quant. Spectrosc. Radiat. Transfer* **2006**, *101*, 249–262.
16. Larson, G.W.; Shakespeare, R.A. *Rendering with Radiance*; Morgan Kaufmann Publishers: San Francisco, CA, USA, 1998.
17. *Radiance Systhetic Imaging System. Radiance Download*. Available online: http://radsite.lbl.gov/radiance/framed.html (accessed on 1 March 2010).
18. Ward, G.J. Measuring and modeling anisotropic reflection. *ACM SIGGRAPH Comput. Graphics* **1992**, *26*, 265–272.
19. Chatten, A.J.; Barnham, K.W.J.; Buxton, B.F.; Ekins-Daukes, N.J.; Malik, M.A. Novel quantum dot concentrators. In *Proceedings* of the 17th European Photovoltaic Solar Energy Conference, Munich, Germany, 22–26 October 2001; pp. 200–203.
20. Chatten, A.J.; Barnham, K.W.J.; Buxton, B.F.; Ekins-Daukes, N.J.; Malik, M.A. Quantum dot solar concentrators. *Semiconductors* **2004**, *38*, 609–617.
21. Chandrasekhar, S. *Radiative Transfer*; Clarendon Press: Oxford, UK, 1950; pp. 1–20.
22. Tan, S.G.; Lim, Y.S.; Lo, C.K.; Ramesh, S. Research and development of luminescent solar concentrators (LSC) in Malaysia. In Proceedings of the 2010 International Conference on Green Energy Technology and Management, Chang-hua, Taiwan, 5–6 June 2010; pp. 15–23.
23. Kubin, R.F.; Fletcher, A.N. Fluorescence quantum yields of some rhodamine dyes. *J. Lumin.* **1983**, *27*, 455–462.

## Appendix A

The radiant power $dP_{rad}$ illuminating an infinitesimal area $dA$ at a position r on the solar cell's surface over an infinitesimal solid angle $d\Omega$, having an angle $\theta$ measured from the surface normal is:

$$d^2P_{rad}(r) = L(\theta,\varphi)\cos\theta d\Omega dA \tag{A.1}$$

where:

$L(\theta,\varphi)$ = Radiance (radiant power per solid angle per unit projected area) (W $m^{-2}$ $sr^{-1}$);

$\theta$ = Polar angle measured from the surface normal (rad);

$\varphi$ = Azimuthal angle measured about the surface normal (rad);

$\Omega$ = Solid angle (sr);

$r$ = Position, $r(x,y,z)$ (m).

Therefore the irradiance at r can be found by integrating Equation (A.1) over a hemisphere:

$$E(r) = \frac{dP_{rad}(r)}{dA} = \int_{\Omega=2\pi} L(\theta,\varphi)\cos\theta d\Omega \tag{A.2}$$

where:

$E(r)$ = Irradiance illuminating the solar cell's surface (W $m^{-2}$).

The integration in Equation (A.2) can be approximated by:

$$E(r) = \int_{\Omega=2\pi} L(\theta,\varphi)\cos\theta d\Omega \approx \sum_{m=1}^{M} W_L^m L^m \tag{A.3}$$

Assuming $L^m$ is centered in a sub-solid angle $\Delta\Omega^m$ and is isotropic over $\Delta\Omega^m$ [10], then:

$$\begin{aligned} E(r) &= \int_{\Omega=2\pi} L(\theta,\varphi)\cos\theta d\Omega \\ &\approx L^1 \int_{\Omega=\Delta\Omega^1} \cos\theta d\Omega + L^2 \int_{\Omega=\Delta\Omega^2} \cos\theta d\Omega + \ldots \\ &+ L^m \int_{\Omega=\Delta\Omega^m} \cos\theta d\Omega + \ldots + L^M \int_{\Omega=\Delta\Omega^M} \cos\theta d\Omega \end{aligned} \tag{A.4}$$

and the right hand side of Equation (A.3) is:

$$\begin{aligned} \sum_{m=1}^{M} W_L^m L^m &= L^1 W_L^1 + I^2 W_L^2 + \ldots \\ &+ L^m W_L^m + \ldots + I^M W_L^M \end{aligned} \tag{A.5}$$

Comparing Equation (A.4) and Equation (A.5), the weight can be found by:

$$\begin{aligned} W_L^m &= \int_{\Omega=\Delta\Omega^m} \cos\theta d\Omega = \int_{\varphi^l-\frac{\Delta\varphi^l}{2}}^{\varphi^l+\frac{\Delta\varphi^l}{2}} \int_{\theta^k-\frac{\Delta\theta^k}{2}}^{\theta^k+\frac{\Delta\theta^k}{2}} \cos\theta\sin\theta d\theta d\varphi \\ &= \frac{1}{4}\left[-\cos\left(2\theta^k+\Delta\theta^k\right)+\cos\left(2\theta^k-\Delta\theta^k\right)\right]\Delta\varphi^l \\ &= \left[\sin\theta^k\cos\theta^k\sin\left(\Delta\theta^k\right)\right]\Delta\varphi^l \end{aligned} \tag{A.6}$$

The value of each $L^m$ can be found by running the "rtrace" program to trace the ray passing through $r(x,y,z)$ from a direction opposite to $(\theta^k,\varphi^l)$, $k$ =1, 2,…, $M_\theta$, $l$ = 1, 2,…, $M_\varphi$:

$$\theta^k = (2k-1)\frac{\pi/2}{2M_\theta}, \quad k = 1,2,...,M_\theta \tag{A.7}$$

$$\Delta\theta^k = \frac{\pi/2}{M_\theta} \tag{A.8}$$

$$\varphi^l = (2l-1)\frac{2\pi}{2M_\varphi}, \quad l = 1,2,...,M_\varphi \tag{A.9}$$

$$\Delta\varphi^l = \frac{2\pi}{M_\varphi} \tag{A.10}$$

where:

$M_\theta$ = Number of discrete $\theta$,

$M_\varphi$ = Number of discrete $\varphi$.

Equations (A.11), (A.12) and (A.13) calculate a list of normalized direction vectors in Cartesian coordinate which cover a hemisphere on a plane with normal vector $\mathbf{N}=\begin{pmatrix}0 & 0 & 1\end{pmatrix}^T$ :

$$\Theta_x^m = \sin\theta^k\cos\varphi^l \tag{A.11}$$

$$\Theta_y^m = \sin\theta^k\sin\varphi^l \tag{A.12}$$

$$\Theta_z^m = \cos\theta^k \tag{A.13}$$

For the particular orientation of solar cell's surface as shown in Figure 4, all the direction vectors should be rotated by $\theta_{\text{rot}} = 94°$ around the axis $\mathbf{A}=\begin{pmatrix}0 & -1 & 0\end{pmatrix}^T$ using Equation (A.14), due to the different normal vector of the sampling plane:

$$\begin{bmatrix}\Theta_x^{m\prime}\\ \Theta_y^{m\prime}\\ \Theta_z^{m\prime}\end{bmatrix} = \begin{bmatrix}M_{11} & M_{12} & M_{13}\\ M_{21} & M_{22} & M_{23}\\ M_{31} & M_{32} & M_{33}\end{bmatrix}^{-1}\begin{bmatrix}N_1\\ N_2\\ N_3\end{bmatrix} \tag{A.14}$$

where:

$$N_1 = (\mathbf{C}\cdot\mathbf{C})\cos(\theta_{\text{rot}}) \tag{A.15}$$

$$N_2 = 0 \tag{A.16}$$

$$N_3 = (\mathbf{C}\cdot\mathbf{C})\sin(\theta_{\text{rot}}) \tag{A.17}$$

$$\begin{pmatrix}M_{11} & M_{12} & M_{13}\end{pmatrix} = (\mathbf{C}\cdot\mathbf{C})^T \tag{A.18}$$

$$\begin{pmatrix}M_{21} & M_{22} & M_{23}\end{pmatrix} = \left(\hat{\mathbf{A}}\right)^T \tag{A.19}$$

$$\begin{pmatrix}M_{31} & M_{32} & M_{33}\end{pmatrix} = \left(\hat{\mathbf{A}}\times\mathbf{\Theta}^m\right)^T \tag{A.20}$$

$$\hat{\mathbf{A}} = \frac{\mathbf{A}}{\|\mathbf{A}\|} \tag{A.21}$$

$$\mathbf{B} = \frac{\mathbf{\Theta}^m \cdot \mathbf{A}}{\mathbf{A} \cdot \mathbf{A}} \hat{\mathbf{A}} \tag{A.22}$$

$$\mathbf{C} = \mathbf{\Theta}^m - \mathbf{B} \tag{A.23}$$

The vector $\mathbf{\Theta}^m = \begin{pmatrix} \Theta_x^m & \Theta_y^m & \Theta_z^m \end{pmatrix}^T$ is the original direction vector, $\mathbf{\Theta}^{m\prime} = \begin{pmatrix} \Theta_x^{m\prime} & \Theta_y^{m\prime} & \Theta_z^{m\prime} \end{pmatrix}^T$ is the direction vector after the rotation, $\theta_{\text{rot}}$ is the rotation angle.

The irradiance at $r(x,y,z)$ is approximated by the weighted sum in Equation (A.3), where $L^m$ is the radiance value returned by the rtrace program, and the weight $W_L{}^m$ is calculated using Equation (A.6):

$$E(r) \approx \sum_{m=1}^{M} W_L^m L^m \left( r, \mathbf{\Theta}^{m\prime} \right) \tag{A.24}$$

The total radiant power illuminating the solar cell's surface can be found by integrating the radiance at r over the surface area of the solar cell:

$$P_{\text{rad(total)}} = \int_{A_{sc}} E(r) \mathrm{d}A \tag{A.25}$$

The integration in Equation (A.25) can be approximated in a similar way by:

$$P_{\text{rad(total)}} = \int_{A_{sc}} E(r) \mathrm{d}A \approx \sum_{n=1}^{N} W_E^n E^n \tag{A.26}$$

Assuming $E^n$ is centered in a small area $\Delta A^n$ and is constant over $\Delta A^n$, then:

$$\begin{aligned} P_{\text{rad(total)}} = \int_{A_{sc}} E(r) \mathrm{d}A \approx E^1 \int_{\Delta A^1} \mathrm{d}A + E^2 \int_{\Delta A^2} \mathrm{d}A + \ldots \\ + E^n \int_{\Delta A^n} \mathrm{d}A + \ldots + E^N \int_{\Delta A^N} \mathrm{d}A \end{aligned} \tag{A.27}$$

The right hand side is:

$$\begin{aligned} \sum_{n=1}^{N} W_E^n E^n = E^1 W_E^1 + E^2 W_E^2 + \ldots \\ + E^n W_E^n + \ldots + E^N W_E^N \end{aligned} \tag{A.28}$$

and the weights can be found by comparing Equation (A.27) and Equation (A.28):

$$W_E^n = \int_{\Delta A^n} \mathrm{d}A = \int_{z^j - \frac{\Delta z^j}{2}}^{z^j + \frac{\Delta z^j}{2}} \int_{y^i - \frac{\Delta y^i}{2}}^{y^i + \frac{\Delta y^i}{2}} \mathrm{d}y\mathrm{d}z = \Delta y^i \Delta z^j \tag{A.29}$$

The value of each $E^n$ can be found by repeating the process that approximates $E(r)$ at one point $r(x,y,z)$ until the points covers every combination of $(y^i,z^j)$, $i = 1, 2,\ldots, M_y$, $j = 1, 2,\ldots, M_z$:

$$y^i = (2i-1)\frac{W}{2M_y}, \quad i = 1,2,...,M_y \tag{A.30}$$

$$\Delta y^i = \frac{W}{M_y} \tag{A.31}$$

$$z^j = (2j-1)\frac{D}{2M_z}, \quad j = 1,2,...,M_z \tag{A.32}$$

$$\Delta z^j = \frac{D}{M_z} \tag{A.33}$$

where:

$M_y$ = Number of discrete points along $y$ direction;

$M_z$ = Number of discrete points along $z$ direction.

The position vector $\mathbf{r}^n = \begin{pmatrix} x^n & y^n & z^n \end{pmatrix}^T$ can be calculated from the list of ($y^j$,$z^j$) by:

$$x^n = L + \delta x + \left(D - z^j\right)\tan\left(\theta_{\text{tilt}}\right) \tag{A.34}$$

$$y^n = y^i \tag{A.35}$$

$$z^n = z^j \tag{A.36}$$

where $\delta x$ is the small gap from the edge of LSC to the sampling plane. For the simulation in Section 4.0, $\delta x$ = 0.00055 m, $\theta_{\text{tilt}}$ = 4°.

The total irradiance is approximated by the weighted sum in Equation (A.26), where the weight is calculated for the list of ($y^j$,$z^j$) using Equation (A.29):

$$P_{\text{rad(total)}} \approx \sum_{n=1}^{N} W_E^n E^n\left(\mathbf{r}^n\right) \tag{A.37}$$

The average irradiance collected by the sampling plane is:

$$E_{\text{average}} = \frac{P_{\text{rad(total)}}}{WD} \tag{A.38}$$

The steps above evaluate the output irradiance at a single wavelength. To get the spectrum output they are repeated for all wavelength of interest. It is done by changing the radiance value of the incident light, refractive index of LSC, absorption coefficient of the mist type material (extinction coefficient with albedo equals to zero) and refractive index of solar cell for the particular wavelength and then repeating the steps above. The results in Section 5.0 were obtained using $M_\theta$ = 630, $M_\varphi$ = 2520, $M_y$ = 1, $M_z$ = 20.

## Appendix B

The two-flux thermodynamic model by Chatten *et al.* [19] solves the radiative transfer equation [21] in one dimensional plane parallel case. The differential equation is split into four coupled equations depending on the polar angle, which are the trapped and escape flux propagating upward, and trapped and escape flux propagating downward. By solving the radiative transfer equation and applying the boundary condition, one would obtain the following solutions.

Solution for the trapped flux:

$$I_T(z) = \frac{\Omega_2 \lambda_{Te} \cosh(\lambda_{Ta} z)}{4\pi \sinh(\lambda_{Ta} D)} \times \int_0^D \cosh\left[\lambda_{Ta}(D - z')\right] B(z')\, dz' - \frac{\Omega_2 \lambda_{Te}}{4\pi} \int_0^z \sinh\left[\lambda_{Ta}(z - z')\right] B(z')\, dz' \quad \text{(B.1)}$$

Solution for the escaped flux:

$$I_E(z) = \frac{2I_1 \sinh(\alpha_T / 2) \cosh\left[\lambda_{Ea}(D - z) + \alpha_B / 2\right]}{\sinh(\lambda_{Ea} D + \alpha_{TB})} + \frac{\Omega_1 \lambda_{Ee} \cosh(\lambda_{Ea} z + \alpha_T / 2)}{4\pi \sinh(\lambda_{Ea} D + \alpha_{TB})} \times \int_0^D \cosh\left[\lambda_{Ea}(D - z') + \alpha_B / 2\right] B(z')\, dz' - \frac{\Omega_1 \lambda_{Ee}}{4\pi} \int_0^z \sinh\left[\lambda_{Ea}(z - z')\right] B(z')\, dz' \quad \text{(B.2)}$$

where the symbols in Equations (B.1) and (B.2) are:

$$\lambda_{Te} = \frac{2N\sigma_e}{\cos(\theta_C)} \quad \text{(B.3)}$$

$$\lambda_{Ta} = \frac{2N\sigma_a}{\cos(\theta_C)} \quad \text{(B.4)}$$

$$\lambda_{Ee} = \frac{N\sigma_e}{\cos^2(\theta_C / 2)} \quad \text{(B.5)}$$

$$\lambda_{Ea} = \frac{N\sigma_a}{\cos^2(\theta_C / 2)} \quad \text{(B.6)}$$

$$\Omega_1 = 4\pi(1 - \cos\theta_C) \quad \text{(B.7)}$$

$$\Omega_2 = 4\pi\cos\theta_C \quad \text{(B.8)}$$

$$\alpha_T = -\ln(R_T) \quad \text{(B.9)}$$

$$\alpha_B = -\ln(R_B) \quad \text{(B.10)}$$

$$\alpha_{TB} = \frac{\alpha_T + \alpha_B}{2} \quad \text{(B.11)}$$

$\Omega_1$ is the solid angle extended by two escape cones in steradians and $\Omega_2$ is the solid angle for trapped flux in steradians. $\sigma_e$ is the absorption cross section of dye in $m^2$, $\sigma_a$ is the absorption cross section of sample in $m^2$.

The value of $R_B$ is the reflection coefficient of unpolarized light averaged over the solid angle of the bottom escape cone, and is calculated by:

$$R_B = \frac{1}{\Omega_C}\int_0^{2\pi}\int_0^{\theta_C} R_{\text{bottom}}(\theta)\sin\theta \mathrm{d}\theta \mathrm{d}\varphi \tag{B.12}$$

where:

$$\Omega_C = 2\pi(1-\cos\theta_C) \tag{B.13}$$

$$R_{\text{bottom}}(\theta) = \frac{1}{2}\left[\left(\frac{\sin(\theta-\theta_t)}{\sin(\theta+\theta_t)}\right)^2 + \left(\frac{\tan(\theta-\theta_t)}{\tan(\theta+\theta_t)}\right)^2\right] \tag{B.14}$$

$$\theta_t = \sin^{-1}\left[\frac{n}{n_{\text{air}}}\sin\theta\right] \tag{B.15}$$

$\Omega_C$ is the solid angle extended by one escape cone in steradians, $n_{\text{air}}$ is the refractive index of air and $n$ is the refractive index of the LSC. $R_T$ is the reflection coefficient over the top escape cone and is calculated in the same way as $R_B$. In the case where mirror is attached to the bottom surface of LSC, then $R_B = 1$.

From 3D thermodynamic model [12], the horizontal photon flux escape from the edge surface at $x = 0$ is:

$$\begin{aligned} I_{\text{Left}}(y,z) &= \frac{\Omega_C \lambda_{Ee}}{2\pi}\frac{\sinh(\alpha_L/2)}{\sinh(\lambda_{Ea}L+\alpha_{LR})} \\ &\times\int_0^L \cosh\left[\lambda_{Ea}(L-x')+\alpha_R/2\right]B(z)\mathrm{d}x' \end{aligned} \tag{B.16}$$

Since we are using two-flux model to calculate the dye emission, $B$ is a function of $z$ only. The equation can be further simplified to:

$$\begin{aligned} I_{\text{Left}}(y,z) &= \frac{\Omega_C \lambda_{Ee}}{2\pi}\frac{\sinh(\alpha_L/2)}{\sinh(\lambda_{Ea}L+\alpha_{LR})} \\ &\times B(z)\int_0^L \cosh\left[\lambda_{Ea}(L-x')+\alpha_R/2\right]\mathrm{d}x' \end{aligned} \tag{B.17}$$

$$\begin{aligned} I_{\text{Left}}(y,z) &= \frac{\Omega_C \lambda_{Ee}}{2\pi\lambda_{Ea}}\frac{\sinh(\alpha_L/2)}{\sinh(\lambda_{Ea}L+\alpha_{LR})} \\ &\times B(z)\left[\sinh(\lambda_{Ea}L+\alpha_R/2)-\sinh(\alpha_R/2)\right] \end{aligned} \tag{B.18}$$

Total optical power received by the surface can be found by integrating over the *yz*-plane:

$$\begin{aligned} I_{\text{Left}} &= \int_0^D\int_0^W \frac{\Omega_C \lambda_{Ee}}{2\pi\lambda_{Ea}}\frac{\sinh(\alpha_L/2)}{\sinh(\lambda_{Ea}L+\alpha_{LR})}B(z') \\ &\times\left[\sinh(\lambda_{Ea}L+\alpha_R/2)-\sinh(\alpha_R/2)\right]\mathrm{d}y'\mathrm{d}z' \end{aligned} \tag{B.19}$$

$$I_{\text{Left}} = \frac{\Omega_C \lambda_{Ee}}{2\pi \lambda_{Ea}} \frac{\sinh(\alpha_L / 2)}{\sinh(\lambda_{Ea} L + \alpha_{LR})} \times \left[\sinh(\lambda_{Ea} L + \alpha_R / 2) - \sinh(\alpha_R / 2)\right] \times \int_0^W \mathrm{d}y' \int_0^D B(z')\,\mathrm{d}z' \tag{B.20}$$

Therefore, the average irradiation spectrum escape from the left surface is:

$$I_{\text{Left(average)}}(v) = \frac{I_L}{WD} \tag{B.21}$$

$$I_{\text{Left(average)}} = \frac{\Omega_C \lambda_{Ee}}{2\pi D \lambda_{Ea}} \frac{\sinh(\alpha_L / 2)}{\sinh(\lambda_{Ea} L + \alpha_{LR})} \times \left[\sinh(\lambda_{Ea} L + \alpha_R / 2) - \sinh(\alpha_R / 2)\right] \times \int_0^D B(v, z')\,\mathrm{d}z' \tag{B.22}$$

where:

$$\alpha_L = -\ln(R_L) \tag{B.23}$$

$$\alpha_R = -\ln(R_R) \tag{B.24}$$

$$\alpha_{LR} = \frac{\alpha_L + \alpha_R}{2} \tag{B.25}$$

$R_L$ and $R_R$ are calculated in the same way as $R_B$. For the case where mirror is attached to the opposite edge of the photovoltaic cells, $R_R = 1$.

The escape flux from the output of thermodynamic model is in the domain of frequency, which can be converted to photon flux in the domain of wavelength by:

$$\Phi_{\text{thermo}}(\lambda) = -I_{L\text{average}}(v)\frac{c}{v^2} \tag{B.26}$$

The negative sign is not used in the actual calculation, since it merely indicates that the order of integration limit is changed from ($v_1$,$v_2$) to ($\lambda_2$, $\lambda_1$), where $v_1 = c/\lambda_1$ and $v_2 = c/\lambda_2$. If $v_1 < v_2$ and since $c$ is always positive, it must be the case where $\lambda_1 > \lambda_2$, then:

$$\int_{v_1}^{v_2} \mathrm{d}v = \int_{\lambda_1}^{\lambda_2} \mathrm{d}\lambda = -\int_{\lambda_2}^{\lambda_1} \mathrm{d}\lambda \tag{B.27}$$

The smaller frequency in thermodynamic model is always used as the lower limit of integration, but in ray tracing and solar cell model the smaller wavelength is always used as the lower limit of integration. Therefore the change in the order of integration limit while changing the domain of integration from frequency to wavelength introduces a negative in the equation, which cancels out the negative sign in Equation (B.26).

Similarly, the incident spectrum obtained from sampling using ray tracing can be converted to frequency domain by:

$$\begin{aligned} I_1(v) &= -E_{\text{average}}(\lambda)\left(\frac{\lambda}{hc}\right)\left(\frac{c}{\lambda^2}\right) \\ &= -E_{\text{average}}(\lambda)\left(\frac{1}{h\lambda}\right) \end{aligned} \tag{B.28}$$